# A novel approach to MP-PIC
## Continuum particle model for dense particle flows in fluidized beds

Verma, Vikrant; Padding, Johan T.

**DOI**
10.1016/j.cesx.2019.100053

**Publication date**
2020

**Document Version**
Final published version

**Published in**
Chemical Engineering Science: X

Chemical Engineering Science: X 6 (2020) 100053

Contents lists available at ScienceDirect

Chemical Engineering Science: X

journal homepage: www.elsevier.com/locate/cesx

# A novel approach to MP-PIC: Continuum particle model for dense particle flows in fluidized beds

Vikrant Verma *, Johan T. Padding *

*Process and Energy Department, Delft University of Technology, Leeghwaterstraat 39, 2628 CB Delft, The Netherlands*

ARTICLE INFO

*Article history:*
Received 28 September 2019
Received in revised form 11 November 2019
Accepted 30 November 2019

*Keywords:*
Discrete Element Model (CFD-DEM)
Continuum Particle Model (CFD-CPM)
Multiphase Particle-in-cell (MP-PIC)
Particle stresses
Coarse-grained simulations
Fluidized beds

ABSTRACT

A novel approach to Multiphase-Particle-in-Cell (MP-PIC), called Continuum Particle Model (CPM), is developed for dense gas-particle flows. CPM has high computational speed, comparable to that of MP-PIC, but a robustness and accuracy closer to that of a Discrete Element Model (DEM). The gas phase is treated as a continuum phase and particles are tracked discretely, but particle collisions are modelled by considering the divergence of the continuum particle stress tensor. Details on efficient solution to the model are presented. For comparison, a parametric study is performed for quasi-2D fluidized beds. Comparison of CFD-CPM is made with MP-PIC and CFD-DEM. The particle stress models by Harris and Crighton, and by Srivastava and Sundaresan are tested in our CFD-CPM. Results from CFD-CPM based on the Srivastava and Sundaresan particle stress model show good agreement with CFD-DEM results. We validate our model by comparison with experimental benchmark results from Gopalan et. al. (2016).


## 1. Introduction

Fluidized beds are widely applied in the chemical, petrochemical, metallurgical, environmental and energy industries due to their favourable mass and heat transfer characteristics (Kunii and Levenspiel, 1991). The complex hydrodynamics of fluidized beds has been extensively studied numerically and experimentally. Due to computational complexities and challenges in experimental measurements, fluidized beds studies are usually limited to a small scale set-up. Information from a small scale reactor is used to predict the hydrodynamics in a large scale reactor. However failure has been reported (Squires, 1982) with this principle, as flow structures in large scale reactors are quite different from those observed in a small scale reactor (Verma et al., 2015). Therefore the study of sufficiently large scale fluidized beds is important. New coarse-grained model developments are of vital importance for the advancement of large-scale modelling of gas-particle flows. In the past few decades, the role of computational fluid dynamics to predict the hydrodynamics of gas-solid fluidized beds has increased considerably. A multi-scale modelling approach has been adopted to study micro and macro characteristics of gas-particle flows (Van der Hoef et al., 2006). The Euler-Lagrange Computational Fluid Dynamics-Discrete Element Model (CFD-DEM) (Tsuji et al., 1993; Deen et al., 2007) is effective and has proved to me more accurate in the modelling of gas-particle flows. In CFD-DEM the fluid phase is treated as a continuum and the individual particles are traced using Newton's second law of motion to update the particle positions and velocities. The gas-particle interactions have to be calculated from effective drag correlations. To account for particle-particle and particle-wall collisions, a standard soft-sphere collision model is usually used (Tsuji et al., 1993), which includes energy dissipation and friction. The particle-particle collisions are fully resolved, which necessitates using a very small time step. DEM is typically limited to a few tens of thousands of particles per processor. The evaluation of the forces on the particles is usually the most time-consuming part of CFD-DEM simulations because this involves calculating the interaction between all neighboring pairs of particles. The amount of computations are lowered by using a neigbourlist which contains the close neighbours of each particle. However, when the number of particles is very large, even generating a neighbour list by evaluating all pair distances is computationally demanding. The concept of a cell-linked list can then be used to optimize the generation of a neighbour-list or even for the direct calculation of particle interactions. Recent improvements in computer hardware have allowed for an increase in the number of solid particles (Jajcevic et al., 2013; Govender et al., 2016; Norouzi et al., 2017). However the available computational resources are often still too limited to be able to study truly large-scale gas-particle flows. When it is not feasible to resolve every individual particle collision due to the large number of

* Corresponding authors.
*E-mail addresses:* dr.v.vikrant@gmail.com, v.vikrant@tudelft.nl (V. Verma), J.T.Padding@tudelft.nl (J.T. Padding).

https://doi.org/10.1016/j.cesx.2019.100053
2590-1400/

particles, the effects of collisions should be modelled with an averaged approach, with an appropriate particle collision closure relation.

The Two-Fluid model (TFM) (Ding and Gidaspow, 1990; Kuipers et al., 1992; Verma et al., 2013) and Multiphase Particle-in-Cell (MP-PIC) (Andrews and O'Rourke, 1996; Snider, 2001) method are two common approaches to deal with large numbers of particles. In TFM, both the gas and solids phase are treated as fully interpenetrating continua. The kinetic theory of granular flow (KTGF) is used to describe particle-particle interactions on a more fundamental basis (Gidaspow, 1994). In the KTGF, the particles are assumed to be perfectly smooth, and particle velocity changes in the tangential impact direction are usually neglected. Only the normal impact and rebound velocities of two colliding particles is taken into account using the coefficient of normal restitution. The TFM is fast, but limited to spherical particles and not-too-dense flows of nearly-elastic particles. The reason for this limitation is that the Eulerian particle updates depend on theoretical expressions for the solid stress and granular temperature, usually based on the KTGF. In the KTGF far-reaching assumptions are made to make the theoretical calculations tractable, such as particle sphericity and isotropy, molecular chaos (no pre-collisional velocity correlations) and binary interactions. However, it is known that correlations in the velocities build up in denser flows (Balzer, 2000), and multiple simultaneous particle contacts can no longer be ignored for particles with finite stiffness. The two-fluid approach has trouble modeling flows with particle type and size distributions because separate continuity and momentum equations must be solved for each size and type (Van Sint Annaland et al., 2009). While a continuous-fluid description of the solids phase has application in some solid-fluid flow regimes, it is inaccurate in others. For dilute solid flows, closure models based on the assumption of high collision frequencies are questionable. Moreover, the non-linear behaviour of some solid flows is difficult to model with a Navier-Stokes momentum equation. In addition, the two-fluid approach cannot easily take into account the shape of particles. Most importantly, for non-spherical particles all distribution functions become non-isotropic and the standard kinetic theory can no longer be applied. A new kinetic theory should be developed for non-spherical particles that allows stress transmission through the particle (continuum) phase. The kinetic energy per unit mass (i.e. granular temperature) associated with the fluctuating motion of the non-spherical particles relative to the local average velocity of the particle phase is a topic of current research. Similar to spherical particles, the particle phase stress for non-spherical particles can be expressed in terms of local particle volume fraction, granular temperature and local rate of deformation and orientation of the particles. From our understanding, it is still challenging to establish an accurate hydrodynamic and rheological description for non-spherical particles, i.e. to treat non-spherical particles as a continuum phase.

Another approach to circumvent the limitation on the number of particles that can be simulated, is the parcels of point particles approach developed by Andrews and O'Rourke (1996). In the multiphase particle-in-cell (MP-PIC) method, the fluid phase is treated as a continuum and the particles are traced in a lagrangian fashion, including a parcel approach where each simulated particle represents a large collection of real particles. Each parcel follows Newton's equations of motion, where inter-phase momentum transfer is accounted for by mapping and interpolating quantities back and forth between parcel locations and the Eulerian grid. Particle-particle collisions in MP-PIC are not fully resolved but are derived from particle stresses. For dense phases, the particle stress for spherical particles is given by Harris and Crighton, 1994 and by Srivastava and Sundaresan (2003). The particle stress gradient is difficult to calculate for each particle, but is usually calculated as a gradient on the Eulerian grid and is then interpolated to discrete particles. Lu et al., 2017 compared experimental results with CFD-DEM and MP-PIC from the opensouce code MFiX (Garg and Dietiker, 2013) and the commercial MP-PIC code Barracuda (CPFD) for small scale bubbling fluidized beds. They compared the particle velocity profile and found that only CFD-DEM could predict the rising solid velocity distribution in agreement with experiments. MP-PIC from both MFiX and CPFD from Barracuda predict significant differences in particle velocity. They clearly reported quantitative and qualitative disagreements for a small-scale system between MP-PIC and CFD-DEM results. Similar disagreement with MP-PIC results were reported by Liang et al. (2014), who reported that the MP-PIC version of CPFD predicts a reasonable profile for the solid velocity, but cannot correctly simulate the bubble coalescence phenomena in bubbling fluidized beds. On the basis of their analysis, they suggested improvement in MP-PIC and importantly the particle stress model in MP-PIC.

Therefore in this work we propose a new model, called Computational Fluid Dynamic -Continuum Particle Model (CFD-CPM) for gas-particle flows. The new model grew out of CFD-DEM and MP-PIC models, where now we still treat the particles as discrete but particle-particle collisions are modelled via a continuum approach to obtain collisions forces from solid stress relations. By accounting for particle collisions via a continuum approach, we substantially reduce the computational time which allows us to simulate large numbers of particles efficiently. The main difference with MP-PIC is that our approach (i) is based on a robust measurement of the local rate of solids deformation, which is important for local stress estimates, (ii) uses particle velocity updates that are simply based on the local divergence of the solid stress tensor. Note that to avoid particle over packing, MP-PIC (MFiX-PIC from Garg and Dietiker, 2013) uses complicated ad hoc conditional updates of the particle velocities, depending on whether a particle is moving towards or away from a high density region. Such complicated conditional updates are avoided in our approach. Details on the CFD-CPM model are explained in Section 2.

This paper is organized as follows: first a general description of the continuum particle model for gas-particle flows is given, then details of CFD-CPM are discussed, followed by the numerical approach to solve the governing equations of CFD-CPM including boundary conditions. Then we present a parametric study to quantify the sensitivity of the parameter used in our model. We also present a validation of our model by comparing with experimental and simulations benchmark data from Gopalan et al. (2016) and Lu et al., 2017.

## 2. Continuum particle model

We developed an in-house multiphase Continuum Particle Model (CFD-CPM), the structure of which is in line with CFDEM (Goniva et al., 2010, 2012) using LIGGGHTS (CFD-DEM) where the fluid phase is solved using the OpenFoam Solver (OpenCFD, 2004) and a new solver was developed for the particle phase. The new CFD-CPM model grew out of DEM and MP-PIC models. The MP-PIC model was originally proposed by Andrews and O'Rourke (1996) later improved by Snider (2001); O'Rourke and Snider, 2010. Another version of MP-PIC is available in commercial packages CPFD (Barracuda), DDPM (ANSYS FLUENT) and open source codes MPPICFoam (OpenFoam) and MFiX-PIC (MFiX). We will show that our model CFD-CPM has an improved capability to simulate gas-particle flows. In CFD-CPM, the fluid phase is treated as continuum and particles are treated both as particles and as a continuum. Particles are treated as continuum phase only to capture the effect of particle collisions from the particle stress gradient. The particle stress gradient is difficult to calculate for each

particle. Therefore the particle stress is first calculated for each computational cell and then the numerically estimated stress gradients are interpolated to the discrete particles. Details of the model are sequentially discussed in the following sections.

### 2.1. Governing equations for the gas phase

The fluid-phase hydrodynamics are calculated from the volume-averaged Navier-Stokes equation (Eqs. (1) and (2)) with gas volume fraction $\epsilon_f$, constant gas viscosity $\mu_f$, gas density $\rho_f$, gravity $\mathbf{g}$, fluid stress tensor $\boldsymbol{\tau}_f$ and gas-solid momentum transfer term $\boldsymbol{F}$. The subscript $f$ represents fluid phase. The formulation of gas-solid momentum transfer for CFD-CPM is discussed in the following section.

$$\frac{\partial \epsilon_f \mathbf{u_f}}{\partial t} + \nabla \cdot \left(\epsilon_f \mathbf{u_f} \mathbf{u_f}\right) = 0 \tag{1}$$

$$\frac{\partial \epsilon_f \mathbf{u_f}}{\partial t} + \nabla \cdot \left(\epsilon_f \mathbf{u_f} \mathbf{u_f}\right) - \nabla \cdot \epsilon_f \boldsymbol{\tau}_f = -\frac{\nabla p}{\rho_f} + \epsilon_f \mathbf{g} - \frac{\boldsymbol{F}}{\rho_f} \tag{2}$$

Here the fluid stress tensor, using the unit tensor $\boldsymbol{I}$ and shear viscosity $\mu_f$, and bulk viscosity $\lambda_f$ is given by Eq. (3), where bulk viscosity $\lambda_f$ for gas phase is set to zero.

$$\boldsymbol{\tau}_f = -\left(\lambda_f - \frac{2}{3}\mu_f\right)(\nabla \cdot \mathbf{u_f})\mathbf{I} - \mu_f\left(\nabla \mathbf{u_f} + (\nabla \mathbf{u_f})^T\right) \tag{3}$$

#### 2.1.1. Formulation of gas-solid momentum transfer

By switching from the discrete particle description to a continuum description we define the inter-phase momentum transfer term $\boldsymbol{F}$ (in Eq. (2)) which contains both momentum transfer due to drag and buoyancy, given by Eq. (4). Here $V_{cell}$ is the volume of the computational cell, $V_p$ the volume of the particle and $\nabla p_i$ the locally averaged fluid pressure gradient evaluated at the location of particle $i$.

$$\boldsymbol{F} = \sum_i \boldsymbol{f}_i = \frac{1}{V_{cell}} \sum_i \left(\boldsymbol{f}_{drag} - V_p \nabla p_i\right) = \boldsymbol{F}_{drag} - \frac{1}{V_{cell}} \sum_i V_i \nabla p_i \tag{4}$$

In a continuum description we can write $\frac{1}{V_{cell}} \sum_i V_i \nabla p_i = (1 - \epsilon_f)\nabla p$ and rewrite Eq. (2) as Eq. (5) by substituting $\boldsymbol{F}$ from Eq. (4).

$$\frac{\partial \epsilon_f \mathbf{u_f}}{\partial t} + \nabla \cdot \left(\epsilon_f \mathbf{u_f} \mathbf{u_f}\right) - \nabla \cdot \epsilon_f \boldsymbol{\tau}_f = -\frac{\epsilon_f \nabla p}{\rho_f} + \epsilon_f \mathbf{g} - \frac{\boldsymbol{F}_{drag}}{\rho_f} \tag{5}$$

$\boldsymbol{F}_{drag}$ is the drag force on particles due to fluid flow (relative to the particles) in a computational grid cell, given by Eq. (6) as a function of inter-phase momentum transfer coefficient $\beta$ and slip velocity $(\mathbf{u_i} - \mathbf{u_f}|_i)$, where $\mathbf{u_i}$ is the particle velocity and $\mathbf{u_f}|_i$ is the fluid velocity interpolated to the position of particle $i$, $w_{ic}$ is the interpolation operator for interpolating properties from particle position $i$ to a computational cell $c$. The momentum transfer coefficient from Gidaspow (1994) is used in this study. The Gidaspow drag model is a combination of the Wen and Yu (1996) and the Ergun (1952). Note that in Eq. (5) $\boldsymbol{F}_{drag}$ is not fully a source term since the drag is proportional to the slip velocity.

$$\boldsymbol{F}_{drag} = \frac{1}{(1 - \epsilon_f) V_{cell}} \sum_i w_{ic} V_i \beta (\mathbf{u_i} - \mathbf{u_f}|_i) \tag{6}$$

Another way of incorporating buoyancy via the pressure gradient is by explicitly adding a local acceleration term and an adjustment to the drag (OpenCFD (2004)) as:

$$\begin{aligned} \boldsymbol{F} &= \frac{1}{V_{cell}} \sum_i \left(\frac{\boldsymbol{f}_{drag}}{\epsilon_f} - \rho_f V_i \left(\mathbf{g} - \left[\frac{D\mathbf{u_f}}{Dt}\right]_i\right)\right) \\ &= \frac{\boldsymbol{F}_{drag}}{\epsilon_f} + \frac{1}{V_{cell}} \sum_i \rho_f V_i \left(\mathbf{g} - \left[\frac{D\mathbf{u_f}}{Dt}\right]_i\right) \end{aligned} \tag{7}$$

where $\left[\frac{D\mathbf{u_f}}{Dt}\right]_i$ is the locally averaged fluid acceleration at the location of particle $i$. Using the fact that the gravity field is uniform and using $\frac{1}{V_{cell}} \sum_i \rho V_i \mathbf{g} = (1 - \epsilon_f)\rho_f \mathbf{g}$ we take this term out of the interaction term and we can write Eq. (2) as:

$$\frac{\partial \epsilon_f \mathbf{u_f}}{\partial t} + \nabla \cdot \left(\epsilon_f \mathbf{u_f} \mathbf{u_f}\right) - \nabla \cdot \epsilon_f \boldsymbol{\tau}_f = -\frac{\nabla p}{\rho_f} + \mathbf{g} - \frac{\boldsymbol{F}_{drag}}{\epsilon_f \rho_f} - \frac{1}{V_{cell}} \sum_i V_i \left[\frac{D\mathbf{u_f}}{Dt}\right]_i \tag{8}$$

using the continuity equation and product rule we get:

$$\frac{D\mathbf{u_f}}{Dt} - \nabla \cdot \epsilon_f \boldsymbol{\tau}_f = -\frac{\nabla p}{\rho_f} + \mathbf{g} - \frac{\boldsymbol{F}_{drag}}{\epsilon_f \rho_f} \tag{9}$$

Multiplying Eq. (9) by $\epsilon_f$ should give same equation as (5), however it is not. Omitting the viscous fluid stresses would result in Eqs. (9) and (5) being equal. Neglecting the laminar fluid viscous terms generally has a negligible effect on dense particle flows, and laminar terms can easily be included in the fluid equation set (Snider, 2001). Another approach to line up Eqs. (9) and (5) is to distribute the viscous fluid stress in the same way the pressure is accounted for in both the fluid phase momentum equation and the particle momentum transfer term:

$$\frac{\partial \epsilon_f \mathbf{u_f}}{\partial t} + \nabla \cdot \left(\epsilon_f \mathbf{u_f} \mathbf{u_f}\right) - \nabla \cdot \boldsymbol{\tau}_f = -\frac{\nabla p}{\rho_f} + \epsilon_f \mathbf{g} - \frac{\boldsymbol{F}}{\rho_f} \tag{10}$$

$$\boldsymbol{F} = \boldsymbol{F}_{drag} - \frac{1}{V_{cell}} \sum_p V_i (\nabla p_i + \nabla \cdot \boldsymbol{\tau}_i) \tag{11}$$

combining the above Eqs. (10) and (11) we end up with:

$$\epsilon_f \frac{D\mathbf{u_f}}{Dt} - \epsilon_f \nabla \cdot \boldsymbol{\tau}_f = -\epsilon_f \frac{\nabla p}{\rho_f} + \epsilon_f \mathbf{g} - \frac{\boldsymbol{F}_{drag}}{\rho_f} \tag{12}$$

Similarly if we use Eq. (2) we can follow the same steps when incorporating buoyancy via the local acceleration and we obtain Eq. (13) instead of Eq. (9). Multiplying Eq. (13) by $\epsilon_f$, gives the same equation as (5), which is consistent.

$$\frac{D\mathbf{u_f}}{Dt} - \nabla \cdot \boldsymbol{\tau}_f = -\frac{\nabla p}{\rho_f} + \mathbf{g} - \frac{\boldsymbol{F}_{drag}}{\epsilon_f \rho_f} \tag{13}$$

In literature the CFD-DEM momentum equation has been derived by two different approaches; the Jackson (1963) approach, in which the viscous stress has a fluid fraction term outside the divergence term, but also includes the effect of viscous stress in the particle momentum equation; and secondly the Ishii (1975) approach in which the fluid fraction is inside the divergence of the viscous stresses but not included in the particle equations. These two approaches are known as Model A and Model B, and cause some amount of confusion when the formulation is used in discrete and continuum two fluid model approaches. In our model we implemented and validated both approaches.

### 2.2. Particle phase

In CFD-CPM all particles are treated as discrete particles, where the position and velocity of each particle is traced. Newton's equations of motion are integrated using the force on each particle. The force $\boldsymbol{F}_i$ on particle $i$ is calculated using Eq. (14). The first two terms on the RHS are the contribution from fluid induced forces, i.e. buoyant force on particle $i$, driven by macroscopic pressure gradients in the surrounding fluid, and the drag force due to the slip velocity *i.e.* the difference between the local (interpolated) fluid velocity and particle velocity. The third term is the force due to gravity. The fourth term takes into account the particle-particle

interaction *i.e.* force due to neighbouring particles. The fluid induced forces are well defined in the literature (Deen et al., 2007), which are treated in similar fashion as in CFD-DEM.

$$\boldsymbol{F}_i = m_i \frac{d\boldsymbol{u}_i}{dt} = V_i \nabla p_f \Big|_i + \frac{V_i \beta}{\epsilon_f}\left(\boldsymbol{u}_f\Big|_i - \boldsymbol{u}_i\right) + m_i \mathbf{g} + \boldsymbol{F}_{p-p} \tag{14}$$

The main difference between CFD-CPM and CFD-DEM resides in the calculation of $\boldsymbol{F}_{p-p}$. In DEM this force is calculated by modelling particle-particle collisions through a linear spring-mass viscous damped system in normal and tangential directions. Details of particle-particle contact forces in DEM can for instance be found in (Tsuji et al., 1993; Deen et al., 2007). In CPM the particle-particle contact forces are modelled from the divergence of the particle stresses (which include both deviatoric stress and pressure terms). The idea which resulted in the CPM is to apply these continuum expressions directly to discrete particles. Details on the force obtained from the particle stress divergence are given in the following section. A similar approach of treating particle collisions from the particle pressure gradient was adopted in the MP-PIC approach by Snider (2001). However, in MP-PIC particle velocities are explicitly calculated from the particle pressure gradient with the goal to estimate the relative motion of the particle. To avoid particle over packing, MP-PIC uses complicated ad hoc conditional updates of the particle velocities, depending on whether a particle is moving towards or away from a high density region. In contrast, CFD-CPM uses particle velocity updates that are simply based on the local divergence of the solid stress tensor.

*2.2.1. Particle stresses*

Particle stresses originate from compressive, shearing and elongational deformations of the particle suspension. Forces between particles caused by compression lead to an isotopic particle pressure and bulk viscous stress, while forces between particles caused by volume conserving deformation lead to particle shear stresses and normal stress differences. Expressions for particle pressure and stresses are given in Table 1. For dilute systems the particle pressure is predicted by kinetic theory (Lun et al., 1984). For dense systems, a frequently used particle pressure model is given by (Harris and Crighton, 1994). This expression only considers the particle volume fraction $\epsilon_s$, and neglects the physical details of the particles and the effect of shearing or elongational deformations. The particle pressure is more important in the dense regime near the close packing limit. The contribution from particle viscous stresses have been ignored so-far in MP-PIC models, where only the particle pressure expression from (Harris and Crighton, 1994) is used. However, besides particle pressure forces, there may also be frictional forces acting on particles when they try to slide past each other in shearing or elongational motion. Calculating such viscous stresses is challenging, since it involves calculating the particle bulk and shear viscosity and the locally averaged particle velocity gradient $< \nabla \mathbf{u}_s >$. One option is to use the particle shear and bulk viscosity as predicted by KTGF based on the local volume fraction and granular temperature. However solving for the granular temperature is not the scope of this work and will be a future extension of this work. Here we focus on the viscous stresses in the dense limit. Srivastava and Sundaresan (2003) derived particle stresses for dense solid suspensions, making use of a critical state pressure $p_c(\epsilon_s)$ and an effect of strain rate fluctuations on the frictional stresses to calculate the frictional viscosity. Their expression is given in Table 1. In their equation, the addition of a term $\frac{\Theta}{d_p^2}$ avoids a numerical singularity in the region where $\mathbf{S} : \mathbf{S}$ approaches zero as long as the granular temperature is non-zero. Note that the granular temperature in dense regions is generally very small. Here we calculate the granular temperature $\Theta$ from the mean fluctuating particle velocity as given in Table 1, where the mean particle velocity $\overline{\mathbf{u}}_s$ in a computational cell is calculated from all particles in the cell. The expression for the critical pressure $p_c(\epsilon_s)$ is given equation by Johnson and Jackson (1987), which is modified to remove the singularity at close packing by adding the $\theta$ expression in the denominator. The $\theta$ is a small number of the order of $10^{-7}$. This approach of removing the singularity from the Harris and Crighton model was also adopted by Snider (2001). The particle stress is unaffected by this modification except when the volume fraction is close to close packing. The close pack limit is somewhat arbitrary and depends on the size, shape, and ordering of the particles. Now the challenge is to calculate the particle velocity gradient in a fluid cell. Because all particle positions and velocities are known within a computational grid cell, the particle velocity gradient can be calculated very efficiently from Eq. (15), where **G** and **C** are the gyration tensor and position-velocity correlation tensor of all $N$ particles present in the computational grid cell, given by Eqs. (16) and (17) respectively. Here $\mathbf{r}_i$ and $\mathbf{v}_i$ are the position and velocity of particle $i$, whereas M is the total mass of particles in the computational grid cell, $\mathbf{R}_{cm}$, and $\mathbf{V}_{cm}$ are the center of mass of position and velocity of all particles present within the computational grid cell. These expressions simplify for systems of particles with equal mass. Note that the tensor **G** and **C** individually are biased by the shape of the cell. For example, in a homogeneously filled cell more particles are present in cell diagonal directions than along the lattice direction. Fortunately this bias is exactly cancelled by combining **C** with the inverse of **G**. This makes the method of estimating the solids velocity gradient also amenable to more complicated cell shapes.

**Table 1**
Particle shear stresses.

$$\boldsymbol{\tau}_s = P_s \mathbf{I} - 2\epsilon_s \mu_s \mathbf{S}$$

Harris and Crighton (1994):

$$P_s = \frac{P^* \epsilon_s^\beta}{max(\epsilon_{max} - \epsilon_s, \delta(1-\epsilon_s))}$$

Lun et al. (1984):

$$P_s = (1 + 2(1+e_n)\epsilon_s \rho_s g_0)\epsilon_s \rho_s \Theta$$

Srivastava and Sundaresan (2003):

$$\boldsymbol{\tau}_s = P_c \mathbf{I} - P_c \sqrt{2}\sin\phi \frac{\mathbf{S}}{\sqrt{\mathbf{S}:\mathbf{S} + \frac{\Theta}{d^2}}}$$

where:

$$\mathbf{S} = \frac{1}{2}\left(< \nabla \mathbf{u}_s > + < \nabla \mathbf{u}_s >^T\right) - \frac{1}{3}(\nabla \cdot \mathbf{u}_s)\boldsymbol{I}$$

$$\Theta = \frac{1}{3} < \mathbf{u}_s^2 - \overline{\mathbf{u}}_s^2 >$$

$$P_c = \begin{cases} Fr \frac{[\epsilon_s - \epsilon_{min}]^r}{[max(\epsilon_{s,max} - \epsilon_s, \theta(1-\epsilon_f))]^s}, & \epsilon_s > \epsilon_{min} \\ 0 & \epsilon_s \leqslant \epsilon_{min} \end{cases}$$

$$< \nabla \boldsymbol{u}_s >= \mathbf{G}^{-1} \cdot \mathbf{C} \tag{15}$$

$$\mathbf{G} = \frac{1}{M}\sum_{i=1}^{N} m_i(\mathbf{r}_i - \mathbf{R}_{cm})(\mathbf{r}_i - \mathbf{R}_{cm}) \tag{16}$$

$$\mathbf{C} = \frac{1}{M}\sum_{i=1}^{N} m_i(\mathbf{r}_i - \mathbf{R}_{cm})(\mathbf{v}_i - \mathbf{V}_{cm}) \tag{17}$$

Note that the expression by Srivastava and Sundaresan (2003) takes into account both particle pressure and viscous stresses for the dense regime, giving rise to two separate forces i.e. from particle pressure and from viscous stresses. We have modelled these forces as discussed in Section 2.2.1. We have implemented and compared both particle pressure from Harris and Crighton (1994) and particle stresses from Srivastava and Sundaresan (2003).

### 2.3. Mapping and interpolation

In CFD-CPM quantities from the Eulerian grid are needed at particle locations, and vice versa. We refer to 'mapping' when considering particle properties transferred to the Eulerian grid cell and to 'interpolation' when considering grid cell quantities estimated at particle locations. Since a collocated grid is used, a single mapping/interpolation scheme is implemented in a generic way that can be applied for quantities of any tensorial rank (scalar, vector or tensor). Interpolation from fluid cell values to the particle location is needed for the local fluid velocity $\mathbf{u}_g|_i$, local pressure gradient $\nabla p_g|_i$, particle stress divergence $\nabla \cdot \sigma_s|_i$ and the interpolated volume fraction fields $\epsilon_f$ and $\epsilon_s$. Mapping of quantities from the particle location is equivalent to defining a weight for the particle with respect to the fluid cell. This is used to determine the particle drag coefficient in Eq. (6), as well as for construction of the solid volume fraction from particle locations. We distinguished two different mapping categories: mapping based on the actual space the particle is occupying or smearing out the influence of the particle on the surrounding cells, not taking into account the physical space occupied by the particle. The latter one is suitable for when the cell size is large compared to particle diameter. In the former case when cell size is in range of the particle diameter, the intersection of a grid cell with the particle is calculated (Deen et al., 2007). To enhance the computational speed CFD-CPM is preferred for a sufficiently large grid cell therefore interpolation schemes are used to weight the contribution of the particle within the computational grid cell.

We implemented trilinear interpolation and mapping schemes. In trilinear interpolation, quantities at particle locations are determined as weighted averages of the eight surrounding cell points (Snider, 2001). For mapping an inverse-trilinear scheme is implemented. Interpolation and mapping near to wall boundaries are treated separately. A particle is considered near to the boundary when its center of mass is less than half a cell length away from the boundary. For interpolation near the boundary, the fields (such as velocity, pressure) are defined on the boundary and a barycentric interpolation scheme from openFoam is applied. For mapping, a folding approach is applied (Link, 2006). In the folding approach a particle will contribute to the surrounding cells, but if such a cell is outside the domain, it is folded back on the Eulerian grid where the boundary is the folding line.

### 2.4. Numerical implementation

For the fluid phase, the OpenFoam flow solver is used to solve the Navier-Stokes Eqs. (1) and (2). A separate repository for CFD-CPM is created, importing the fluid phase (CFD) solver from openFoam and coupling it with the newly developed particle phase solver (CPM). We use a regular rectangular mesh for both the gas and (continuum)-particles phase. We note that a different mesh could be used for the gas phase and particles phase with appropriate interpolation and mapping functions when transferring information. In OpenFoam the Navier-Stokes equations are approximated by finite volumes with a collocated grid, where scalar, vectors and tensor variables are defined on the cell center. The collocated grid gives rise to the checkerboard problem when using a central differencing scheme. This problem is handled using the Rhie-Chow interpolation scheme. The advantage of using a collocated scheme is the use of only single cell center interpolation operators for mapping particle properties to and from the grid cells. The discretised form of the momentum equation is solved using the PIMPLE algorithm, a combination of PISO and SIMPLE. Since pressure and velocity are implicitly coupled in the Navier-Stokes equations, a pressure-velocity decoupling algorithm is used. The fluid solver from OpenFoam uses the GAMG (Generalised Geometric-algebraic multi-grid) matrix solver. For more details on the fluid phase solver readers are referred to OpenFoam (OpenCFD, 2004).

In the Navier-Stokes equations the gas void fraction $\epsilon_f$ is obtained from the particle phase calculations $\epsilon_f = 1 - \epsilon_s$. The particle volume fraction $\epsilon_s$ for cell $c$ is given by Eq. (18), where $w_{ic}$ is the mapping operator for particle $i$ in cell $c$ and $N_P$ is the number of particles influencing the value of the particle volume fraction in cell $c$. Details on interpolation and mapping are given in Section 2.3. The inter-phase momentum transfer term is treated in a semi-implicit fashion, *i.e.* split into an explicit and implicit part as given by Eq. (19), where superscripts "*" and "**" represent quantities at new and old time-step respectively. Setting these quantities leads to the numerical solution of the Navier-Stokes equations for fluid velocity and pressure fields.

$$\epsilon_s = \frac{1}{V_{cell}}\sum_{i}^{N_p} V_i w_{ic} \tag{18}$$

$$\boldsymbol{F}^{*}_{drag} = \frac{1}{V_{cell}}\sum_{i}^{N_p} w_{ij}\frac{V_i\beta}{\epsilon_s}\left[\mathbf{v}_i^{**} - \left(\mathbf{u}_f^{**}\Big|_i - \mathbf{u}_f^{**}\right)\right] - \frac{1}{V_{cell}}\sum_{i}^{N_p} w_{ij}\frac{V_i\beta}{\epsilon_s}\mathbf{u}_f^{*} \tag{19}$$

Given the fluid velocity and pressure field over the domain, the particle positions are updated knowing the particle velocity (Eq. (20)). The velocity of the particle is calculated from integration of the forces acting on it (Eq. (14)). However the continuum particle-particle collision force obtained from the divergence of particle stresses tends to be either dominant or insignificant due to the high non-linearity of the particle stresses. It is highly sensitive to a change in solid volume fraction near to close packing (Snider, 2001). Therefore the continuum force on particles due to solids stresses is treated explicitly. This means that the net particle velocity change can be divided into different parts (Eq. (21)) i.e. an intermediate particle velocity $\mathbf{u}_p^{n\prime}$, and the velocity change due to solid stresses $\mathbf{u}_{p\tau}$. First the intermediate velocity $\mathbf{u}_p^{n\prime}$ is calculated from all acting forces except the force due to particle collisions (solid stresses) (Eq. (14), without the last term). The intermediate velocity $\mathbf{u}_p^{n\prime}$ is computed according to the velocity Verlet algorithm (OpenCFD, 2004) given in Table 2 with those steps applied to all particles. Once the intermediate particle velocities are known, the new solid volume fraction is calculated. Given the updated solid volume fraction, the particle velocity change due to solid stresses $\mathbf{u}_{p\tau}$ is obtained from the gradient of solid pressure $\boldsymbol{\tau}_s^{I}$ and divergence of viscous stresses $\boldsymbol{\tau}_s^{II}$ is interpolated to the particle position.

$$\mathbf{r}_p^{n+1} = \mathbf{r}_p^{n} + \Delta t \mathbf{u}_p^{n+1} \tag{20}$$

$$\mathbf{u}_p^{n+1} = \mathbf{u}_p^{n\prime} + \left(\mathbf{u}_{p\tau_s^{I}} + \mathbf{u}_{p\tau_s^{II}}\right) \tag{21}$$

As explained in Section 2.2 the model from Harris and Crighton (1994) accounts only for the isotropic particle pressure and neglects the viscous stresses, whereas the model from Srivastava and Sundaresan (2003) includes the viscous stress. The particle-particle collision force on a single particle $i$ is given by Eq. (22), where the stress tensor $\boldsymbol{\tau}_s$ is in the form of Eq. (23) and is calculated accordingly from the Srivastava and Sundaresan (2003) model, or from the Harris and Crighton (1994) model (Table 1). Substituting $\boldsymbol{\tau}_s$ in Eq. (22) gives rise to two separate forces on particle $i$ given by Eq. (25).

$$\mathbf{F}_i^{\tau_s} = \left(\frac{m_i}{\epsilon_s \rho_s} \nabla \cdot \boldsymbol{\tau}_s\right)_i \tag{22}$$

$$\boldsymbol{\tau}_s = -p_s \mathbf{I} + 2\epsilon_s \mu_s \mathbf{S} \tag{23}$$

$$= -p_s \mathbf{I} + \epsilon_s \boldsymbol{\sigma} \tag{24}$$

$$\mathbf{F}_i^{\tau_s} = \mathbf{F}_i^{\tau_s^I} + \mathbf{F}_i^{\tau_s^{II}} = -\left(\frac{m_i}{\epsilon_s \rho_s} \nabla p_s\right)_i + \left(\frac{m_i}{\epsilon_s \rho_s} \nabla \cdot \epsilon_s \boldsymbol{\sigma}\right)_i \tag{25}$$

Corresponding to the above force, the particle velocity change due to the solids pressure $\mathbf{u}_{p\tau_s^I}$ is calculated from Eq. (26). The gradient of the solid pressure $\nabla p_s$ is defined on the cell faces while the pressure itself is defined on cell centres. The interpolation operator is used to interpolate the gradient of solid pressure from cell faces to the particle positions i.e. $[\nabla p_s]_i$. The effective particle velocity change $\mathbf{u}'_{p\tau_s^I}$ arising from solid pressure is updated according to Eq. 27, where $\delta\mathbf{u}_i$ is the relative velocity of particle $i$ in the grid cell $\left(\delta\mathbf{u}_i = \mathbf{u}_i - \sum_{\mathbf{j}}^{\mathbf{N_p}} \mathbf{u_j} \mathbf{w_{cj}}\right)$ and $e$ is the coefficient of restitution of the particle. The MinMod operator applied on a particle velocity vector is imported from OpenFoam. The particle velocity change due to the solids pressure $\mathbf{u}_{p\tau_s^I}$ in Eq. 27 is calculated (from Eq. (26)) only when the relative velocity is oriented towards increasing solids volume fraction (*i.e.* $\delta\mathbf{u}_i \cdot \nabla\epsilon_s > 0$) otherwise $\mathbf{u}_{p\tau_s^I}$ is set to zero. Note that the magnitude of particle velocity is calculated taking into account the coefficient of restitution of the particle that define particle-particle collision characteristics. In this way the continuum particle normal stress gradient applied to discrete particle is limited by particle velocity relative to mean flow velocity, and is dominant close to dense particle packing.

Next the forces due to the divergence of the viscous stress tensor are applied to the discrete particles. For this, the forces within each cell are obtained from Gauss theorem (Eq. (28)), transforming the divergence of the stress tensor, integrated over the cell volume, to a simple sum over all cell faces $f$ of the stress tensor contracted with the normal vector $\boldsymbol{S}_f$ (with magnitude equal to the area of that face). Note that is basically going back to the very definition of a stress tensor, as the force per unit area exerted by the phase on one side of an (imaginary) surface on the phase on the other side. The viscous stresses on the cell faces are obtained from simple linear interpolation between the cell nodes adjusted to the faces. Note that the viscous forces on the cell now no longer depend on the stress values of that particular cell, hence avoiding the checkerboard problem. The viscous force on a specific particle $i$ can then be written as a weighted sum with the interpolation function $w_{ci}$ over all the cell $c$ (Eq. (29)). The expression in Eq. (29) is distributing the viscous force experienced within a cell over all particles in or near that cell (depending on the shape of the distribution function). Once the forces on particles due to viscous stresses are known, the corresponding particle velocity $\mathbf{u}_{p\tau_s^{II}}$ is obtained from Eq. (30). The discussed numerical algorithm is performed for each time step. At each time step fluid pressure, volume fraction of gas and solid, fluid velocity, particle velocity, and particle position are updated.

**Table 2**
Velocity-Verlet algorithm.

1. Calculate half velocity implicitly from equation

$$\mathbf{v}_i(t + \Delta t/2) = \frac{\mathbf{v}_i(t) + \frac{1}{2}\Delta t\left(\frac{1}{m_i}\mathbf{F}_i(t) + \frac{V_i\beta}{\epsilon_s m_i}\mathbf{v}_i(t - \Delta t/2)\right)}{1 + \frac{1}{2}\frac{V_i\beta}{\epsilon_s m_i}\Delta t}$$

2. Update position of particle $i$ : $\mathbf{r}_i(t + \Delta t) = \mathbf{r}_i(t) + \mathbf{v}_i(t + \Delta t/2)\Delta t$
3. Given the updated particles position $\mathbf{r}_i(t + \Delta t)$, the new $\epsilon_s$ and $\epsilon_g$ is calculated (only once).
4. Calculate $\mathbf{F}_i(t + \Delta t)$ explicitly from $\mathbf{r}_i(t + \Delta t)$ and $\mathbf{v}_i(t + \Delta t/2)$, i.e.

$$\mathbf{F}_i(t + \Delta t) = -V_i \nabla p_g(t)|_i + \frac{V_i\beta}{\epsilon_s}(\mathbf{u}_g(t)|_i - \mathbf{v}_i(t + \Delta t/2)) + m_i\mathbf{g}$$

where $\beta = \beta(\mathbf{u}_g(t)|_i, \mathbf{v}_i(t + \Delta t/2))$ and $\epsilon_s = \epsilon_s(t + \Delta t)|_i, \epsilon_g = \epsilon_g(t + \Delta t)|_i$, i.e. we use fluid fields from the previous step.
5. Calculate final velocity implicitly

$$\mathbf{v}_i(t + \Delta t) = \frac{\mathbf{v}_i(t + \Delta t/2) + \frac{1}{2}\Delta t\left(\frac{1}{m_i}\mathbf{F}_i(t + \Delta t) + \frac{V_i\beta}{\epsilon_s m_i}\mathbf{v}_i(t + \Delta t/2)\right)}{1 + \frac{1}{2}\frac{V_i\beta}{\epsilon_s m_i}\Delta t}$$

$$\mathbf{u}_{p\tau_s^I} = \frac{-\Delta t[\nabla p_s]_i}{\rho_p \epsilon_s|_i} \tag{26}$$

$$\mathbf{u}'_{p\tau_s^I} = MinMod\left[\mathbf{u}_{p\tau_s^I}, -(1+e)(\delta\mathbf{u}_i)\frac{|\mathbf{u}_i|}{|\delta\mathbf{u}_i|}\right] \tag{27}$$

$$\boldsymbol{F}^{\tau_s^{II}} = \iiint_{V_{cell}} (\nabla \cdot \boldsymbol{\sigma}) \mathrm{d}V = \oiint_{S(V_{cell})} \boldsymbol{\sigma} \cdot \hat{\mathbf{n}} \mathrm{d}S \approx \sum_{\mathrm{f}} \sigma_f \cdot \mathbf{S}_f \tag{28}$$

$$\mathbf{F}_i^{\tau_s^{II}} = \frac{V_i}{\epsilon_s} \sum_{cell} w_{ci} \frac{\boldsymbol{F}^{\tau_s^{II}}}{V_{cell}} \tag{29}$$

$$\mathbf{u}_{p\tau_s^{II}} = \frac{-\Delta t \boldsymbol{F}_i^{\tau_s^{II}}}{m_i} \tag{30}$$

### 2.4.1. Boundary conditions

For wall boundaries, a no slip boundary condition is applied for the fluid phase, whereas particles collide with the wall to prevent them from leaving the domain. Since the desired time-step is relatively large, we can use a hard-sphere collision model for the particle-wall interaction. Details on the hard-sphere model are given in Deen et al. (2007). For instance, consider a particle with velocity $\mathbf{v}_i$. Prior to collision with a wall, the particle velocity can be decomposed in a tangential and normal component relative to the wall, $\mathbf{v}_{i,t}$ and $\mathbf{v}_{i,n}$, respectively. The hard-sphere model is characterized by three collision parameters, the coefficient of normal restitution $e_n$, the coefficient of tangential restitution $\beta_0$ and the coefficient of friction $\mu$. Given these coefficients the velocities after collision with a wall are calculated from Eqs. (31) and (32).

$$\mathbf{v}\prime_{i,n} = -e_n \mathbf{v}_{i,n} \tag{31}$$

$$\mathbf{v}'_{i,t} - \mathbf{v}_{i,t} = \begin{cases} -\frac{2}{7}(1+\beta_0)\mathbf{v}_{i,t}, & \text{if } -\mu(1+e_n)\mathbf{v}_{i,n} \geqslant \frac{2}{7}(1+\beta_0)\mathbf{v}_{i,t}, \\ \mu(1+e_n)\mathbf{v}_{i,n}, & \text{otherwise.} \end{cases} \tag{32}$$

### 2.5. Results and discussions

Test simulations were carried out to show the validity of the model. First we performed a parametric study on a small scale

pseudo −2D bed, and compared the CFD-CPM results with CFD-DEM and MP-PIC (from OpenFoam) simulations. The parametric study is focused to quantify the influence of cell size and particles stress model in CFD-CPM. Next we performed a model validation by comparison against experimental and simulation data from Gopalan et al. (2016) and Lu et al., 2017.

### 2.6. Parametric Study

In this parametric study we quantify the influence of the computational cell size and particles stress models in CFD-CPM on the hydrodynamics of a pseudo 2D fluidized bed. The bed dimensions and particle properties are chosen equal to the case of Goldschmidt et al. (2004). The reason for the choice of a small 2D bed is the feasibility to compare our model with collision resolved DEM simulations. For comparison CFD-DEM simulations were performed using CFDEM (from LIGGGHTS) where the fluid phase is solved using OpenFoam solver. Moreover, we compare our results with MP-PIC simulations, also implemented in OpenFoam. Details of the simulation settings used in CFD-CPM, CFD-DEM, and MP-PIC are given in Table 3. Simulation were performed for a total time of 20 s, and time-averaged data is considered by ignoring the initial 2 s to exclude start-up effects. Comparisons are made on the basis of particle/gas fraction distribution across the bed, average particle bed height, averaged axial particle velocity, and bubble properties such as equivalent bubble diameter, and the bubble distribution. The average particle bed height is calculated from the maximum gradient of porosity as the particle bed enters the free board region. The equivalent bubble diameter in a 2D bed is calculated by area equivalent to a circular bubble, where a gas fraction greater than 0.8 in a cell contributes to the gas bubble. Details on the bubble detection algorithm are given in Verma et al. (2015).

#### 2.6.1. Effect of cell size

CFD models have limitations with respect to the allowable range of grid cell size for accurate simulation predictions. Several researchers (Cloete et al., 2015; Uddin et al., 2017) have studied the influence of cell size on simulations results. In our continuum particle model, quantities related to the solid phase such as drag, solid volume fraction, particle shear stress etc. are calculated for each cell and then interpolated to particle positions. The number of particles in the cell determines not only the gas/solid volume fraction for each cell, but also the statistical accuracy with which solid quantities can be determined. Therefore, the model could be sensitive to the computational cell size. A too coarse cell can smear out the solid particle properties too much while a too fine grid can introduce statistical errors related to a too low number of solid particles per cell, which will influence the interpolation and mapping, as well as the estimate of the local rate of deformation **C**. An optimum choice of cell size is necessary for accurate simulation predictions. Therefore we performed simulations on different cell sizes; the ratio of volume of the cell to the volume of a particle ranged from 10 to 250, assuming 60% of the cell is occupied by particles. This choice of 60% corresponds to a densely packed system where particles stresses are high and therefore most relevant. Fig. 1 shows the average axial particle velocity for different cell sizes at the height of 6 and 12 cm, respectively. Fig. 1a shows that there is no significant difference in the lower region of the particle bed at a height of 6 cm. However, significant difference is observed at the height of 12 cm in Fig. 1b. The average axial particle velocity is lower for both very coarse ($N_P$ = 250) and fine grids ($N_P$ = 15), when compared with CFD-DEM simulations. Moreover a much lower particle velocity near to the wall is observed. This is due to the wall boundary conditions and the uniform mesh sizes in CFD-CPM, which may not be small enough to catch the small-scale wall effects on local hydrodynamics. This is clear because for very fine cell size near to the walls the particle velocity follows a trend similar to that of CFD-DEM simulations. The CFD-DEM simulations predicts a slightly asymmetric axial particle velocity. Yang et al. (2016) also observed such asymmetry in axial particle velocity, the reason for which is explained later when we compare porosity distributions. Overall, the particle velocity at both heights is in good agreement with CFD-DEM simulations, if the cell contains 35 to 55 particles for dense packings. Therefore, the computational domain is divided into 3x15x45 cells, which is equivalent to a maximum of 35 particles in a single cell and is used further in this study.

#### 2.6.2. Effect of solid pressure

The main difference between CFD-CPM and CFD-DEM lies in the treatment of particle-particle interactions as discussed in Sec-

**Table 3**
Simulation settings for parametric study.

| Parameter | CFD-CPM | MP-PIC | CFD-DEM |
|---|---|---|---|
| Depth x-direction (m) | 0.015 | 0.015 | 0.015 |
| Width x-direction (m) | 0.15 | 0.15 | 0.15 |
| Height x-direction (m) | 0.45 | 0.45 | 0.45 |
| Grid Cells (x,y,z) | (3,15,45) | (3,15,45) | (2,30,90) |
| Number of particles | 24,750 | 24,750 | 24,750 |
| Particle diameter (mm) | 2.5 | 2.5 | 2.5 |
| Particle density (kg/m$^3$) | 2526 | 2526 | 2526 |
| $e_n$ (particle-particle) | 0.97 | 0.97 | 0.97 |
| $e_n$ (wall) | 0.97 | 0.97 | 0.97 |
| $\mu$ (wall) | 0.35 | 0.35 | 0.35 |
| $\epsilon_{max}$ | 0.64 | 0.64 | - |
| $\Delta t$ (s) [Fluid] | 2x10$^{-4}$ | 2x10$^{-4}$ | 2x10$^{-4}$ |
| $\Delta t$ (s) [DEM particle] | - | - | $10^{-5}$ |
| Drag model | Gidaspow (1994) | Gidaspow (1994) | Gidaspow (1994) |
| $\mathbf{u}_{inlet}$ (m/s) | 1.875 | 1.875 | 1.875 |
| Particle stress model (HC) | Harris and Crighton (1994) | Harris and Crighton (1994) | - |
| | (P* = 10, $\beta$ =2) | (P* = 10, $\beta$ =2) | - |
| Particle stress model (SS) | Srivastava and Sundaresan (2003) | - | - |
| | (Fr = 0.05 $Nm^{-2}$, r = 2, s = 3 | - | - |
| | $\epsilon_{min} = 0.5, \phi = 28^o$) | - | - |
| Interpolation | Trilinear | Dual Averaging (OF) | - |
| Mapping | Inverse Trilinear | - | - |

tion 2.2.1. Several researchers (Lu et al., 2017; Liang et al., 2014; Yang et al., 2018) have found that the MP-PIC model with the Harris and Crighton (1994) particle pressure model has limitations in simulating dense fluidized beds. These studies concluded that further development and improvement in the particle pressure and stress model is required. In this study, we have implemented the particle stress model by Srivastava and Sundaresan (2003) (SS), as well as the particle pressure model by Harris and Crighton (1994) (HC). The HC model takes into accounts only isotopic pressure, and SS accounts total particle stresses including particles pressure and viscous stresses (see Table 1). The SS model is based on the theory of critical state pressure by Johnson and Jackson (1987), which is activated at a threshold cut-off solid fraction value greater than 0.5. In contrast, the particle pressure from the HC model is applied without any cut-off which means that it is applied for both dilute and dense flow regimes.

### 2.7. Porosity distribution and particle flow patterns

Fig. 2 shows snapshots of instantaneous fluidizing particles from the simulations. Fig. 2a and b are from CPM based on the two particle stress models HC and SS, and Fig. 2c and d are from MP-PIC and CFD-DEM simulations respectively. It is clear that all models show gas bubble formation in the particle bed. For these instantaneous images, shown at a simulation time of 10 s, the qualitative gas-particle flow behaviour is typically similar. However, there are quantitative difference in the bubble characteristics. Details on time-averaged bubbles characteristics will be discussed in this later section. Fig. 3 shows the time averaged porosity distribution predicted from different models. In fluidized beds with spherical particles, bubbles grow near to the wall and move towards the center across the bed height (Verma et al., 2013; Werther, 1974; Werther, 1975). The continuous passage of bubbles through the center leads to a higher porosity distribution in the center of the bed. This phenomenon of a higher porosity distribution in the center is predicted by the CFD-CPM based on SS particle stress and is in good agreement with the more detailed CFD-DEM simulations. In contrast, CFD-CPM based on the HC particle pressure shows nearly homogeneous porosity distribution and the MP-PIC model predicts a very distinct porosity distribution with asymmetric flow behaviour.

The maximum gradient in the average porosity at the height of 0.2 m is indicative of the average particle bed height, where collapsing of bubbles and flashing of particles into the freeboard region occurs. The width of the porosity distribution near the freeboard region indicates the rate with which bubbles gradually burst into the freeboard region. These bubble bursting phenomena near the freeboard are well known for fluidized beds (Kunii and Levenspiel, 1991) and are well predicted by both CFD-DEM and CFD-CPM with the SS particle stress model. In contrast, CFD-CPM with the HC particle pressure model predicts a much sharper transition. This shows that the HC particle pressure model fails to predict the gradual collapse of bubbles into the free-board region. The reason for this will be explained later when we discuss particle bed height and bubble size. A thick solid shear zone near to the side walls is predicted by both CFD-CPM and CFD-DEM simulations. In CFD-DEM, a difference in thick particle shear zone near to the left and right walls leads to a slightly asymmetric particle vertical velocity, as seen in Fig. 1. Yang et al. (2016) observed a similar asymmetry in particle vertical velocity in experiments and in CFD-DEM simulations. This is due to the very narrow depth of a pseudo-2D bed, which has significant influence of walls. The steady particle circulation patterns which develop in a narrow fluidized beds, often show dead particle zones near to the side walls. To develop a perfect symmetry in particle vertical velocity, the particle dead zone near the walls need to be destroyed by fluidizing particles, which usually requires an extremely long period of time.

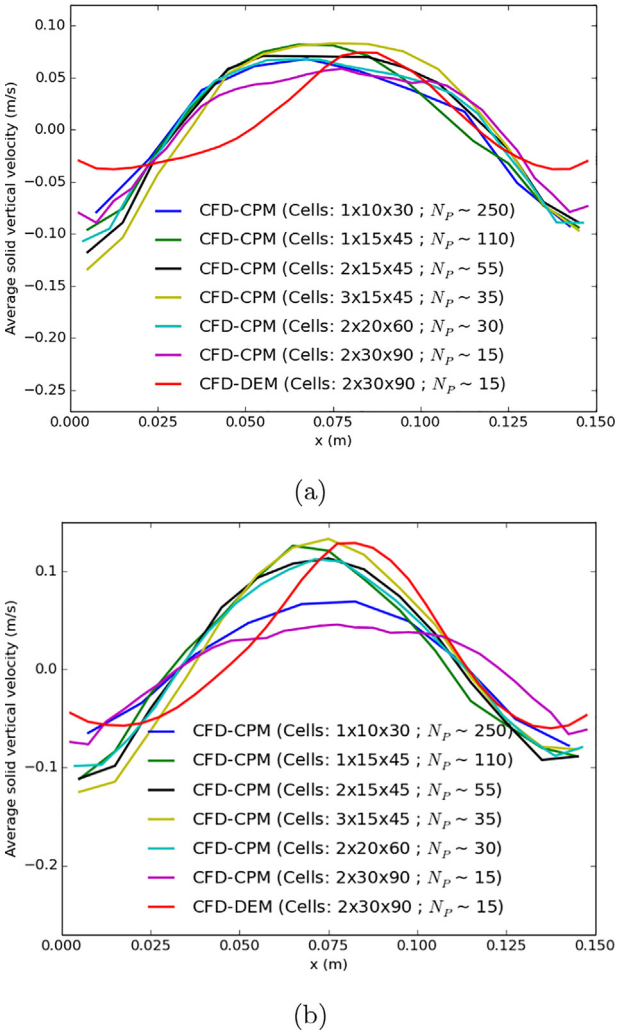


**Fig. 1.** Averaged solid vertical velocity for different cell sizes calculated at a height of (a) 6 cm and (b) 12 cm from the bottom.

The estimation of the time-averaged solid fraction distribution across the bed height is shown in Fig. 4a, where we see that the slope of the curve from CFD-CPM (with the SS model) is in good agreement with CFD-DEM simulations. A slight deviation in solids distribution is predicted in the middle of particle bed ($z \approx 0.1$–$0.15$ m), compared to CFD-DEM simulations. The sharper solid distribution beyond the height of 0.2 m (which is the region of surface of the particle beds) for the HC model is consistent with Fig. 3a. The MP-PIC model predicts a very different solid distribution both in the lower and upper region of the particle bed. The standard deviation from the time averaged solid volume fraction is shown in Fig. 4b. The HC based CPM simulation underestimate the standard deviation of the time averaged volume fraction. This gives evidence of less pronounced bubbling of fluidized beds. The particles are less heterogeneously distributed because of the more diffusive interface of the bubble surface (Schneiderbauer et al., 2013), which is also confirmed by Figs. 2a and 3a. From instantaneous (individual frame) porosity distributions in the bed, we observed that the MP-PIC model predicts regions with unrealistically dense packing of particles near to 75%, which is far beyond the closest random packing of spherical particles. The CFD-CPM model does not display such artefacts.

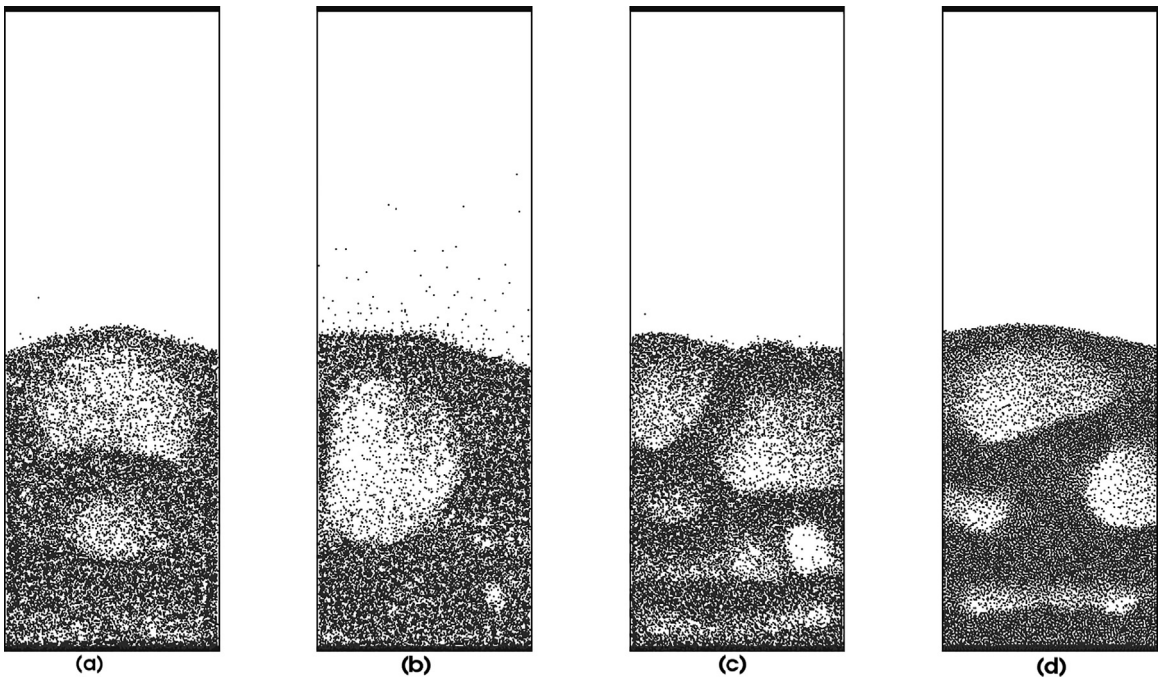


**Fig. 2.** Instantaneous particle distribution at t = 10 s from (a) CFD-CPM ($P_s$:HC) (b) CFD-CPM ($\tau_s$: SS) (c) MP-PIC ($P_s$:HC) (d) CFD-DEM.

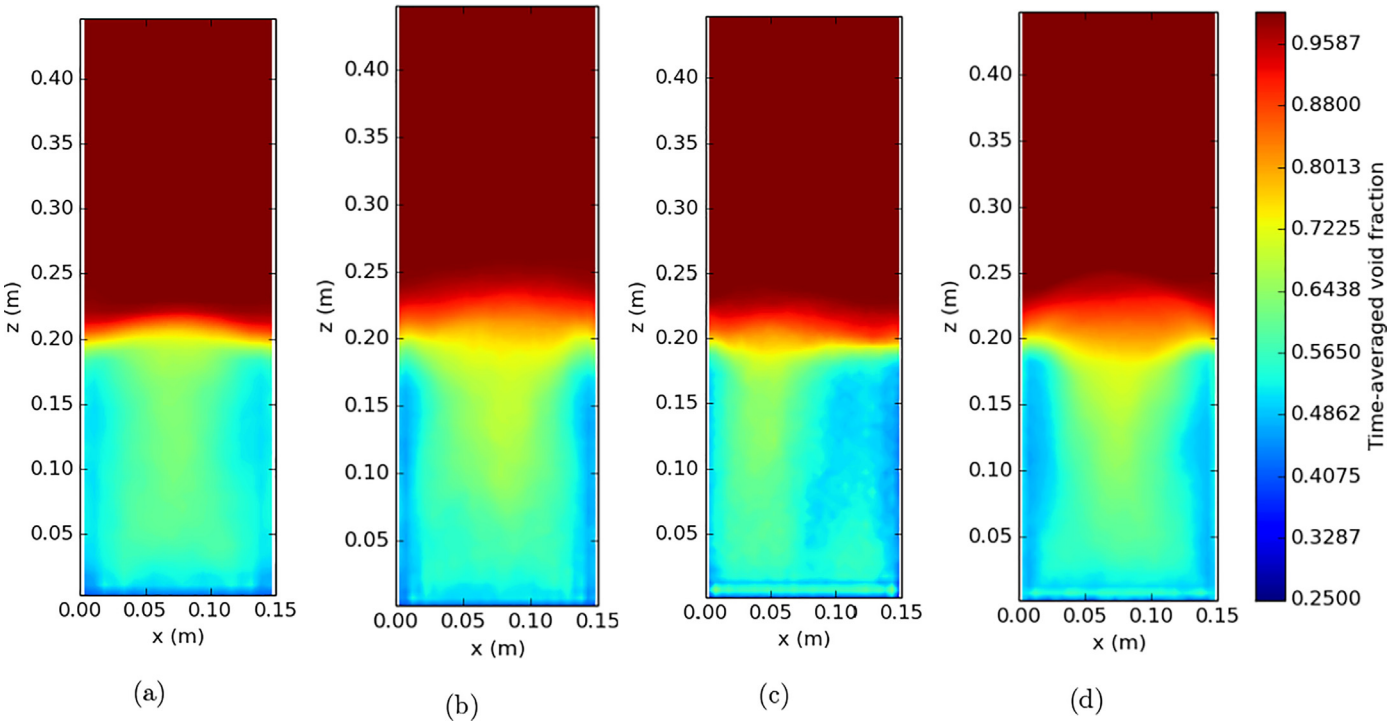


**Fig. 3.** Time-averaged porosity distribution from (a) CFD-CPM ($P_s$:HC) (b) CFD-CPM ($\tau_s$: SS) (c) MP-PIC ($P_s$:HC) (d) CFD-DEM.

Fig. 5 shows the fluctuations in particle bed height with time. The corresponding dashed lines represent the mean particle bed height. For clarity, the fluctuations in bed height are shown from 5 to 10 s, whereas the mean bed height is obtained by averaging over a longer time between 2 and 20 s. The higher and lower amplitudes in fluctuations indicate the presence of larger and smaller bubbles in the bed, respectively. The fluctuations in the instantaneous bed height and the mean bed height predicted by CFD-CPM based on the SS particle stress is in good agreement with the more detailed CFD-DEM simulations whereas MP-PIC and CFD-CPM based on the HC particle pressure predict lower fluctuations and a lower mean bed height. The smaller fluctuations in bed height for HC models are cause by diffusive bubbles that collapse into the freebroad region less violently compared to sharp bubbles. More details on the bubble size

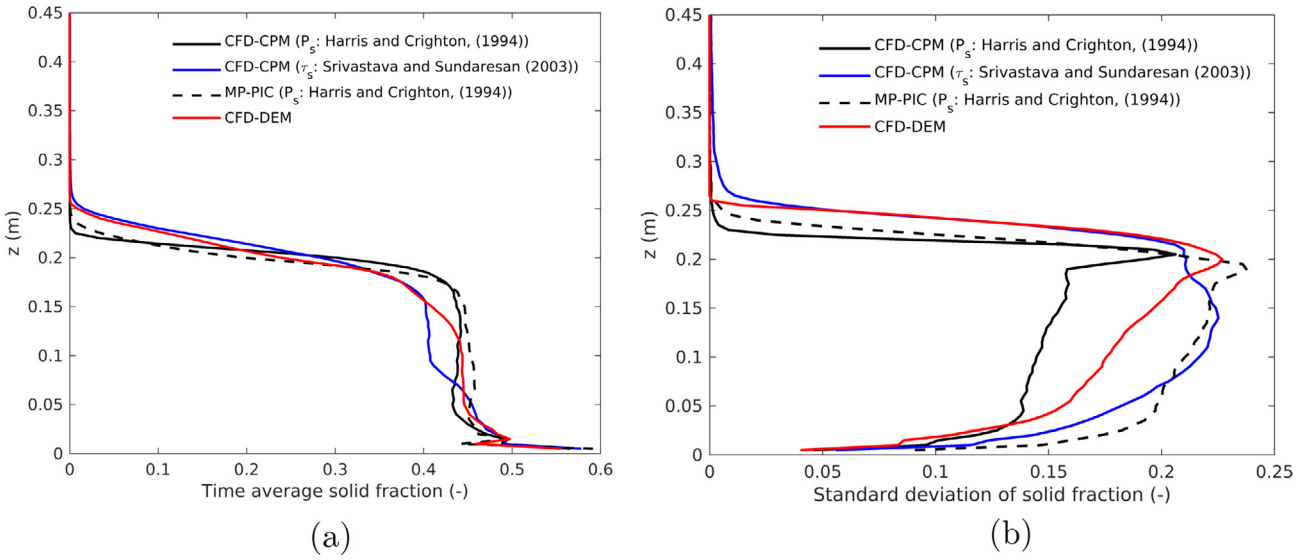


**Fig. 4.** (a) Time-averaged solid volume fraction distribution; (b) Standard deviation from the time-averaged solid volume fraction, as a function of axial position.

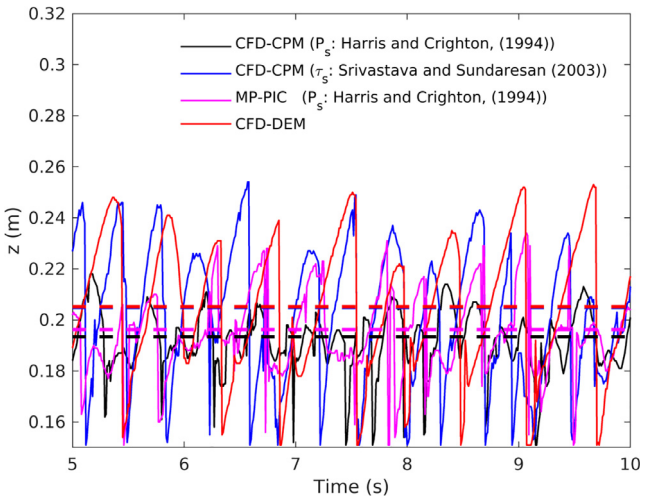


**Fig. 5.** Fluctuations in instantaneous particle bed height. The corresponding dashed line represents mean particle bed height averaged for 2–20 s.

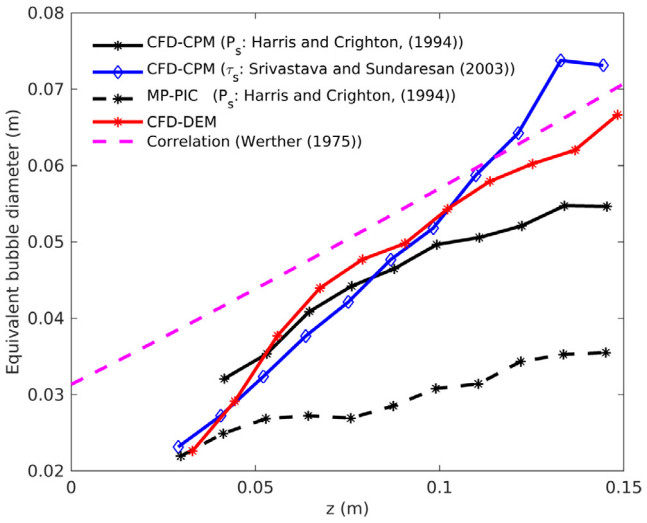


**Fig. 6.** Equivalent bubble diameter as a function of height from different CFD models.

will be discussed in the following section. The horizontal lines for mean bed height from CFD-DEM (red dashed) and CFD-CPM with SS particle stress (black dashed) show such a good agreement that they are overlapping and are difficult to distinguish. These results are consistent with our previous discussion on Fig. 3a–d, where a more gradual change in porosity distribution occurs at a height of 0.2 m. The porosity distribution and beds height are macroscopic measured quantities generally used to quantify the fluidization in a large scale industrial fluidized beds. We can conclude that these quantities are accurately captured by CFD-DEM and CFD-CPM based on the SS particle stress model.

### 2.8. Bubble hydrodynamics

Bubble properties are important characteristics of fluidized beds that define their hydrodynamics. Bubbles grow at the bottom near to the walls and move towards the centre, and due to coalescence these bubbles grow in size while moving upwards through the particles bed (Kunii and Levenspiel, 1991). Many researchers developed correlations for the bubble size for different particle types. Werther (1975) developed a correlation to calculate the bubble size in a fluidized bed at a given excess gas velocity, for different classifications of particles (Geldart A, B, and D). Since our glass particles of 2.5 mm fall in the Geldart D classification, we compared the equivalent bubble diameter predicted from simulations with the (Werther, 1975) correlation suitable for Geldart D particles. Fig. 6 shows that the bubble diameter continuously increases with height in the particle bed. CFD-CPM based on the SS particle stress model predicts a bubble size in good agreement with CFD-DEM simulations. The bubble size from the Werther correlation is generally overpredicting the observed bubble size from the simulations. This is because their correlation did not consider a zero initial bubble size at the bottom which is the case in numerical studies. Note that MP-PIC predicts a much smaller bubble size in comparison to CFD-DEM and CFD-CPM. CFD-CPM based on the HC model underpredicts the bubble size in the higher section of the beds (beyond a height of 0.1 m) this due to the diffusive nature of bubbles that makes it difficult to trace the bubble surface accurately. This is evident from the bubble counts in Fig. 7a, where less

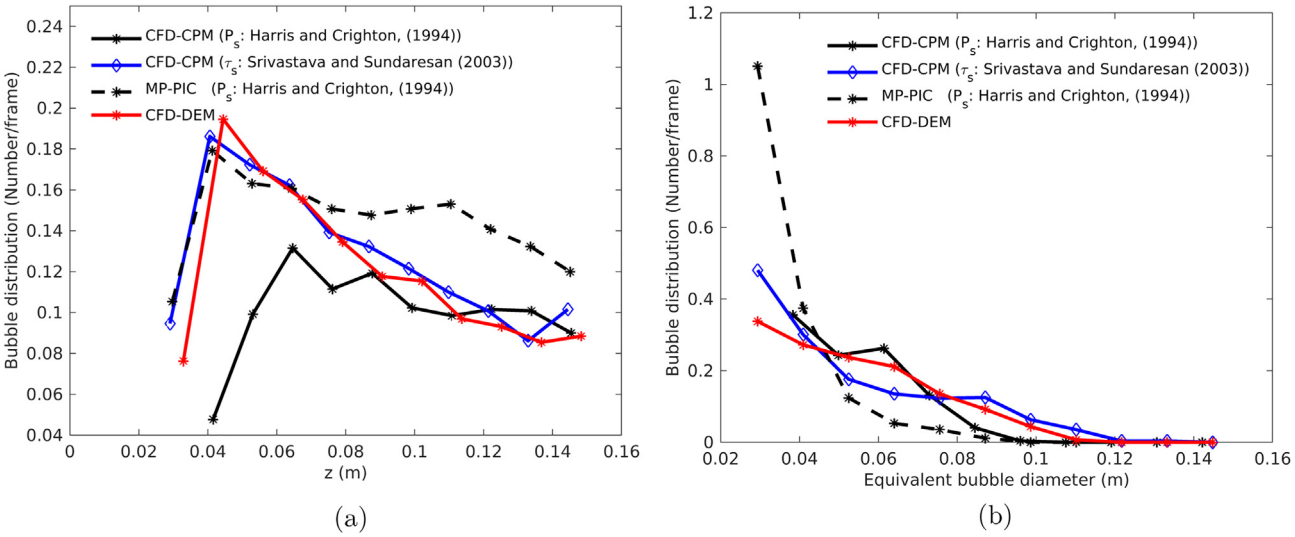


**Fig. 7.** (a) Bubble distribution as a function of height. (b) Bubble distribution as a function of bubble size.

bubbles are detected in the lower section of the bed and bubbles of size less than 3 cm are not detected. Higher in the bed, nearly the same number of bubbles are detected both with HC and SS models but bubbles larger than 9 cm are not predicted by the HS model as revealed from Fig. 7b. CFD-CPM (based on SS particle stresses) and CFD-DEM simulations predict nearly the same number of bubbles statistically (Fig. 7a–b). On the other hand MP-PIC poorly predicts the bubble growth in fluidized beds, where the bubble size shown in Fig. 6 is much lower. This is due to the occurrence of small bubbles throughout the particle bed, as shown in Fig. 7b. It is know that, as bubbles grow in size due to bubble coalescence, they continue to extract gas from the emulsion phase. However the existence of many small bubbles and few large bubble in MP-PIC shows that coalescence of small bubbles to form large bubbles is rare. Similar observations were done by Liang et al. (2014) based on their CPFD (which is MP-PIC with a parcels approach) simulations for bubbling fluidized beds for geldart B particles. They demonstrated that the CPFD model cannot predict the right bubble coalescence mechanism in a bubbling fluidized bed. The bubbles in a fluidized bed by the CPFD model tend to rise to the bed surface vertically. There is no observed bubble coalescence phenomenon even when two bubbles are very near to each other in the same horizontal plane, although coalescence or merging of bubbles occurs for vertically trailing bubbles. That is to say, lateral bubble movement is almost absent. This observation also holds true for our MP-PIC simulations for Geldart D particles, when analysing sequences of images visually.

### 2.9. Average particle velocity

Fig. 8 shows the average axial particle velocity at a height of 6 and 12 cm respectively. This is equivalent to Fig. 1, but now comparing the different methods. An upward motion of particles in the centre and downwards particle motion near to the walls is predicted by both CFD-DEM and CFD-CPM simulations. A slightly asymmetric particle velocity is predicted from simulations due differences in the thick particle shear zone near to the side walls as explained in the previous section for the porosity distribution. The MP-PIC model fails to predict these phenomena of particle motions. A distinct asymmetric motion of particles in the bed

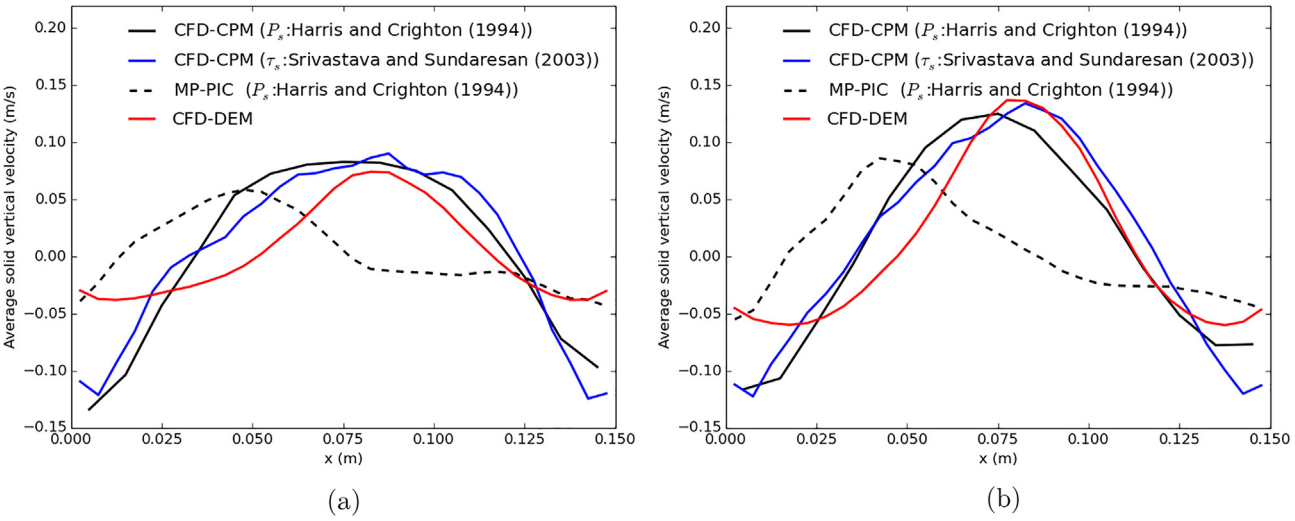


**Fig. 8.** Averaged particle vertical velocity in the bed at a height of (a) 0.06 m and (b) 0.12 m from the bottom.

is observed in MP-PIC. When comparing the magnitude of axial particle velocity from different models, CFD-CPM predicts a particle velocity in agreement with CFD-DEM simulations at both height (Fig. 8a–b). Again the magnitude of axial particle velocity predicted by MP-PIC simulations does not agree with CFD-DEM. In CFD-CPM the axial partial velocity profile near the wall shows a larger deviation at both heights, compared to CFD-DEM. This is due to the difference in wall boundary conditions implementation in CFD-CPM and CFD-DEM, where an approximate hard-sphere model is used in CFD-CPM for collisions of particles with the wall, and a soft sphere model is used in CFD-DEM. Implementing a soft sphere model for particle-wall BC would require a much smaller time step, which is generally to be avoided for such coarse grained models. Moreover, during particle interaction with the wall, the rotation of a particle is ignored in CPM, whereas rotation of a particle is accounted for in DEM modelling. Finally, the uniform mesh sizes in CFD-CPM may not be small enough to catch the small-scale wall effect on local hydrodynamics. This is evident from Fig. 1a and b on cell size effect, where refining the cell size was found to improve the flow near to the wall. Using a small time-step and small cell size is not the scope of CFD-CPM, since this model is geared towards large scale systems, where large cell size and time step are preferred. In future improvements of boundary conditions in CFD-CPM, the collisions between particle and wall could be modelled using similar continuum approaches as used in two-fluid models (Yang et al., 2016).

### 2.10. Comparison between simulations and experimental results

Lu et al. (2017) compared experimental results from the NETL small scale challenge problem (NETL Challenge problem, 2013; Gopalan et al., 2016) with CFD-DEM and MP-PIC from the MFiX code and the commercial MP-PIC based code CPFD Barracuda. We performed simulations for the same set-up, using our CFD-CPM model. Details of the simulation settings for bed dimensions and particle properties are given in Table 4, all other computational settings for CFD-CPM are the same as in Table 3. The averaging of the particle velocity is performed in cells of 0.0457 m width, 0.0457 m height and 0.003 m depth, across the full width (of 0.23 m) of the bed, but constrained in depth to the 3 mm closest to the front wall. This was done to match the experimental setting of Gopalan et al. (2016) and the simulations setting of Lu et al. (2017). Fig. 9 shows that the time-averaged particle velocity from CFD-CPM is in good agreement with the experimental data and CFD-DEM results. In agreement with experiments, CFD-CPM and CFD-DEM predict upward motion of particles in the center and downward near the walls. However MP-PIC from both MFiX and Barracuda predict a flat vertical particle velocity profile (please note that the average upward velocity predicted by MP-PIC can be non-zero because the measurement cells do not span the entire depth of the simulation box). Gopalan et al. (2016) observed that the average particle mass flux (Eulerian averaged) and number averaged particle velocity (Lagrangian averaged) are nearly the same for sufficiently long time averaging. Therefore, the flat vertical particle velocity by MP-PIC could be because of insufficient time averaging for the averaged particle velocity to predict a net up-down flow of particles. Lu et al. (2017) also observed the instantaneous particle distribution and flow patterns and found large slugging bubbles in CFD-DEM simulations, whereas MP-PIC does not show large bubbles in the centre. CFD-CPM is able to predict the large bubbles rising in the centre, leading to a higher axial particle velocity in the center of the bed. This shows the validity of our model to predict particle hydrodynamics accurately.

**Table 4**
Simulation settings for validation against experimental system of NETL challenge problem (2013).

| Parameter | CFD-CPM |
|---|---|
| Depth x-direction (m) | 0.075 |
| Width x-direction (m) | 0.23 |
| Height x-direction (m) | 1.20 |
| Grid Cells (x,y,z) | (4,16,80) |
| Number of particles | 95,000 |
| Particle diameter (mm) | 3.256 |
| Particle density (kg/m$^3$) | 1131 |
| $\mathbf{u}_{inlet}$ (m/s) | 3.28 |
| $e_n$ (particle-particle) | 0.84 |
| $e_n$ (wall) | 0.92 |
| $\mu$ (wall) | 0.35 |
| $\epsilon_{max}$ | 0.64 |

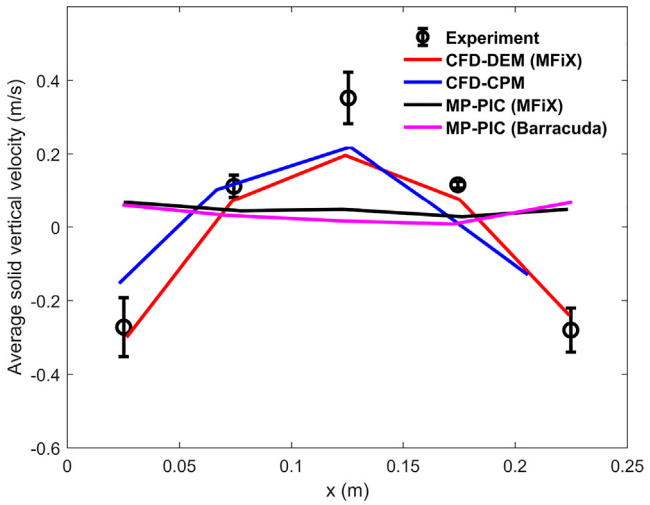


**Fig. 9.** Averaged particle vertical velocity in the bed at the height of 0.0762 m. The experimental, CFD-DEM and MP-PIC simulations data are compared from (Gopalan et al., 2016; Lu et al., 2017) respectively, where the average is performed for the depth of 3.0 mm.

#### 2.10.1. Computational time

Of course, the reason for coarse-graining the particle interactions is to make the computation much faster compared to CFD-DEM simulations. The wall clock computation time on a single Xeon processor, for the setting in Table 3 and 20 s of real time simulations, are as follows: 1.5 h for CFD-CPM and 8.5 h for MP-PIC from OpenFoam. CFD-DEM using CFDEM can only be run on parallel processors, a serial run is not possible with the current version. However assuming a linear scale up in speed, CFD-DEM takes around 18 h on a single processor for 20 s of real time simulations. Therefore CFD-CPM is 12 times faster than CFD-DEM, and 5 times faster than MP-PIC (from OpenFoam).

## 3. Conclusions

In this paper, a novel approach to MP-PIC model is presented. A Computational Fluid Dynamics -Continuum Particle Model (CFD-CPM) is developed and validated to study gas-solid fluidized beds. Comparison of CFD-CPM is made with MP-PIC from OpenFoam and CFD-DEM from CFDEM-LIGGGHTS. Results from CFD-CPM are in good agreement with CFD-DEM, whereas MP-PIC fails to predict the hydrodynamics of fluidized beds. Unrealistic over-packing of solids is predicted in MP-PIC, which does not occur in CFD-CPM. We studied the effects of particle stress correlations and cell size in the newly developed CFD-CPM model. Results from CFD-CPM

based on the particle stress model from Srivastava and Sundaresan (2003) show good agreement with CFD-DEM for fluidized bed hydrodynamics. The particle pressure model from Harris and Crighton (1994) underpredicts the particle and bubble hydrodynamics. The CFD-CPM model is sensitive to the computational cell size, where a cell size containing 35 to 55 particles for dense packing results in a good agreement. In CFD-CPM the average axial particle velocity near to the wall shows larger deviation from CFD-DEM results. This is due to the difference in the wall boundary conditions implementation in CFD-CPM and CFD-DEM. Future improvement of wall boundary conditions in CFD-CPM is suggested by handling the collisions between particles and walls using similar continuum approaches as used in two-fluid models. CFD-CPM has a high computational speed compared to that of MP-PIC and CFD-DEM models. Even for the parcel size 1 studied in this work, meaning that each particle is explicitly modelled, the CFD-CPM is 10–15 times faster with a similar accuracy and robustness as that of CFD-DEM. Future work for the development of CFD-CPM includes a parcel-based scale-up and implementing algebraic form of the granular temperature equation, to calculate the random and dissipative forces originating due to intra-cell particle collisions.

## CRediT authorship contribution statement

The authors declare that they have no known competing financial interests or personal relationships that could have appeared to influence the work reported in this paper.

## Acknowledgements

The authors thank the European Research Council for its financial support, under its consolidator grant scheme, contract No. 615096 (NonSphereFlow).

## References

Andrews, M.J., O'Rourke, P.J., 1996. The multiphase particle-in-cell (MP-PIC) method for dense particulate flows. Int. J. Multiphas Flow 22, 379–402. https://doi.org/10.1016/0301-9322(95)00072-0.

Balzer, G., 2000. Gas-solid flow modelling based on the kinetic theory of granular media: validation, applications and limitations. Powder Technol. 113, 299–309. https://doi.org/10.1016/S0032-5910(00)00313-2.

Cloete, S., Johansen, S.T., Amini, S., 2015. Grid independence behaviour of fluidized bed reactor simulations usingthe Two Fluid Model: Effect of particle size. Powder Technol. 269, 153–165. https://doi.org/10.1016/j.powtec.2014.08.055.

Deen, N.G., Van Sint Annaland, M., Van der Hoef, M.A., Kuipers, J.A.M., 2007. Review of discrete particle modeling of fluidized beds. Chem. Eng. Sci. 62, 28–44. https://doi.org/10.1016/j.ces.2006.08.014.

Ding, J., Gidaspow, D., 1990. A bubbling fluidization model using kinetic theory of granular flow. AIChE J. 36, 523–538. https://doi.org/10.1002/aic.690360404.

Ergun, S., 1952. Fluid flow through packed columns. Chem. Eng. Prog. 48, 89–94.

Gidaspow, D., 1994. Multiphase Flow and Fluidization Continuum and Kinetic Theory Description. Academic Press, Boston.

Goldschmidt, M.J.V., Beetstra, R., Kuipers, J.A.M., 2004. Hydrodynamic modelling of dense gas-fluidised beds: comparison and validation of 3D discrete particle and continuum models. Powder Technol. 142, 23–47. https://doi.org/10.1016/j.powtec.2004.02.020.

Gopalan, B., Shahnam, M., Tucker, J., Shaffer, F., Shadle, L., Mei, J., Rogers, W., Guenther, C., Syamlal, M., 2016. Measurements of pressure drop and particle velocity in a pseudo 2-D rechangular bed with Geldart Group D particles. Powder Technol. 291, 299–310. https://doi.org/10.1016/j.powtec.2015.12.040.

Govender, N., DanielWilke, N.D.N., Kok, S., 2016. Blaze-DEMGPU: Modular high performance DEM framework for the GPU architecture. SoftwareX 5, 62–66. https://doi.org/10.1016/j.softx.2016.04.004.

Goniva, C., Kloss, C., Hager, A., Pirker, S., 2010. An open source cfd-dem perspective. Proceedings of Open FOAM Workshop, Göteborg, 22–24.

Goniva, C., Kloss, C., Deen, N.G., Kuipers, J.A.M., Pirker, S., 2012. Influence of rolling friction on single spout fluidized bed simulation. Particuology 10 (5), 582–591. https://doi.org/10.1016/j.partic.2012.05.002.

Harris, S.E., Crighton, D.G., 1994. Solutions, solitary waves and voidage disturbances in gas-fluidized beds. J. Fluid Mech. 266, 243–276. https://doi.org/10.1017/S0022112094000996.

Ishii, M., 1975. Thermo-Fluid Dynamics Theory of Two-Phase Flow. Eyrolles.

Jackson, R., 1963. The mechanics of fluidized beds. Part I. The stability of the state of uniform fluidization. Trans. Inst. Chem. Eng. 41, 13–21.

Johnson, P.C., Jackson, R., 1987. Frictional–collisional constitutive relations for granular materials, with application to plane shearing. J. Fluid Mech. 176, 67–93. https://doi.org/10.1017/S0022112087000570.

Jajcevic, D., Siegmann, E., Radeke, C., Khinast, J.G., 2013. Large-scale CFD–DEM simulations of fluidized granular systems. Chem. Eng. Sci. 98, 298–310. https://doi.org/10.1016/j.ces.2013.05.014.

Kunii, D., Levenspiel, O., 1991. Fluidization Engineering. Butterworth-Heinemann Inc.

Kuipers, J.A.M., van Duin, K.J., van Beckum, F.H.P., van Swaaij, W.P.M., 1992. A numerical model of gas-fluidized beds. Chem. Eng. Sci. 47, 1913–1924. https://doi.org/10.1016/0009-2509(92)80309-Z.

Liang, Y., Zhang, Y., Li, T., Lu, C., 2014. A critical validation study on CPFD model in simulating gas–solid bubbling fluidized beds. Powder Technol. 263, 121–134. https://doi.org/10.1016/j.powtec.2014.05.003.

Lu, L., Gopalan, B., Benyahia, S., 2017. Assessment of different discrete particle methods ability to predict gas-particle flow in a small-scale fluidized bed. Ind. Eng. Chem. Res. 56, 7865–7876. https://doi.org/10.1021/acs.iecr.7b01862.

Link, J.M., 2006. Development and validation of a discrete particle model of a spout-fluid bed granulator PhD thesis. University of Twente.

Garg, R., Dietiker, J., 2013. Documentation of Open-Source Mfix-pic Software for Gas-Solids Flows. NETL.

NETL Challenge problem, 2013. https://mfix.netl.doe.gov/experimentation/challenge-problems/.

Lun, C.K.K., Savage, S.B., Jeffrey, D.J., Chepurniy, N., 1984. Kinetic theories for granular flow: inelastic particles in Couette flow and slightly in elastic particles in a general flow field. J. Fluid Mech. 140, 223–256. https://doi.org/10.1017/S0022112084000586.

Norouzi, H.R., Zarghami, R., Mostouf, N., 2017. New hybrid CPU-GPU solver for CFD-DEM simulation of fluidized beds. Powder Technol. 316, 233–244.

O'Rourke, P.J., Snider, D.M., 2010. An improved collision damping time for MP-PIC calculations of dense particle fows with applications to polydisperse sedimenting beds and colliding jet particles. Chem. Eng. Sci. 65, 6014–6028.

OpenCFD, 2004. www.OpenFoam.com.

Schneiderbauer, S., Puttinger, S., Pirker, S., 2013. Comparative analysis of subgrid drag modifications fro dense gas-particle flows in bubbling beds. AIChE J. 59 (11), 4077–4099. https://doi.org/10.1002/aic.14155.

Srivastava, A., Sundaresan, S., 2003. Analysis of a frictional-kinetic model for gas-particle flow. Powder Technol. 129, 72–85. https://doi.org/10.1016/S0032-5910(02)00132-8.

Snider, D.M., 2001. An incompressible three-dimensional multiphase particle-in-cell model for dense particle flows. J. Comput. Phys. 170, 523–549. https://doi.org/10.1006/jcph.2001.6747.

Squires, A.M., 1982. Contribution towards a history of fluidization. In: Proceeding of the Joint Meeting of Chemical Engineering Society of China and AIChE. Chemical industry press, Beijing, China, pp. 322–353.

Tsuji, Y., Kawaguchi, T., Tanaka, T., 1993. Discrete particle simulation of two-dimensional fluidized bed. Powder Technol. 77, 79–87. https://doi.org/10.1016/0032-5910(93)85010-7.

Uddin, M.H., Charles, J., Coronella, C.J., 2017. Effects of grid size on predictions of bed expansion in bubbling fluidized beds of Geldart B particles: a generalized rule for a grid-independent solution of TFM simulations. Particuology 34 (2017), 61–69. https://doi.org/10.1016/j.partic.2016.12.002.

Van der Hoef, M.A., Ye, M., van Sint Annaland, M., Andrews, A.T., Sundaresan, S., Kuipers, J.A.M., 2006. Multiscale modeling of gas fluidized beds. Adv. Chem. Eng. 31, 65–149. https://doi.org/10.1016/S0065- 2377(06)31002-2.

Van Sint Annaland, M., Bokkers, G.A., Goldschmidt, M.J.V., Olaofe, O.O., van der Hoef, M.A., Kuipers, J.A.M., 2009. Development of a multi-fluid model for polydisperse dense gas–solid fluidised beds, Part I: Model derivation and numerical implementation. Chem. Eng. Sci. 64, 4222–4236. https://doi.org/10.1016/j.ces.2009.06.044.

Verma, V., Deen, N.G., Padding, J.T., Kuipers, J.A.M., 2013. Two-fluid modeling of three-dimensional cylindrical gas-solid fluidized beds using the kinetic theory of granular flow. Chem. Eng. Sci. 102, 227–245. https://doi.org/10.1016/j.ces.2013.08.002.

Verma, V., Padding, J.T., Deen, N.G., Kuipers, J.A.M., 2015. Effect of bed size on hydrodynamics in 3-D gas-solid fluidized beds. AIChE J. 61, 1492–1506. https://doi.org/10.1002/aic.14738.

Wen, C.Y., Yu, Y.H., 1996. Mechanics of fluidization. AIChE Ser. 62, 100.

Werther, J., 1974. Influence of bed diameter on the hydrodynamics of gas fludized beds. AIChE Symp. Ser. 70, 53–62.

Werther, J., 1975. Bubble growth in a large diameter fluidized beds. International Fluidization Conference, Pacific Grove, USA, 1975. In: Keairns, D.L. (Ed.), Fluidization Technology. Hemisphere Publication Co, Washington DC, pp. 215–235.

Yang, L., Padding, J.T., Kuipers, J.A.M., 2016. Modification of kinetic theory of granular flow for frictional spheres, part II: Model validation. Chem. Eng. Sci. 152, 783–794.

Yang, S., Wu, H., Lin, W., Li, H., Zhu, Q., 2018. An exploratory study of three-dimensional MP-PIC-based simulation of bubbling fluidized beds with and without baffles. Particuology 39, 68–77. https://doi.org/10.1016/j.partic.2017.10.003.

Yang, L., Padding, J.T., Kuipers, J.A.M., 2016. Modification of kinetic theory of granular flow for frictional spheres, part I: two-fluid model derivation and numerical implementation. Chem. Eng. Sci. 152, 767–782. https://doi.org/10.1016/j.ces.2016.05.031.